# Multielectron effects in the photoelectron momentum distribution of noble-gas atoms driven by visible-to-infrared-frequency laser pulses: A time-dependent density-functional-theory approach

Mitsuko Murakami, G. P. Zhang, and Shih-I Chu

Phys. Rev. A **95**, 053419 — Published 26 May 2017

DOI: 10.1103/PhysRevA.95.053419

# Multielectron effects in the photoelectron momentum distribution of noble-gas atoms driven by a visible-to-infrared frequency laser pulses: time-dependent density-functional theoretical approach

Mitsuko Murakami,[1,2,*] G. P. Zhang,[2] and Shih-I Chu[1,3]

[1] *Center for Quantum Science and Engineering, Department of Physics, National Taiwan University, Taipei 10617, Taiwan*

[2] *Department of Physics, Indiana State University, Terre Haute, IN 47809, USA*

[3] *Department of Chemistry, University of Kansas, Lawrence, Kansas 66045, USA*

(Dated: May 1, 2017)

## Abstract

We present the photoelectron momentum distributions (PMDs) of helium (He), neon (Ne) and argon (Ar) atoms driven by a linearly-polarized, visible (527 nm) or near-infrared (800 nm) laser pulse (20 optical cycles in duration), based on the time-dependent density functional theory (TDDFT) under the local density approximation with a self-interaction correction. A set of time-dependent Kohn-Sham equations for all electrons in an atom is numerically solved using the generalized pseudospectral method. An effect of the electron-electron interaction driven by a visible laser field is not recognizable in the He and Ne PMDs except for a reduction of the overall photoelectron yield, but there is a clear difference between the PMDs of an Ar atom calculated with the frozen-core approximation and the TDDFT, indicating an interference of its M-shell wavefunctions during the ionization. Furthermore, we find that the PMDs of degenerate $p$-states are well separated in intensity when driven by a near-infared laser field, so that the single-active-electron approximation can be adapted safely.

* Mitsuko.Murakami@indstate.edu

## I. INTRODUCTION

Since the X-ray free-electron lasers around the world (such as LCLS in US, SACLA in Japan, and the FLASH in Germany) became operational around 2010, many groundbreaking experiments have been conducted in the field of angle-resolved photoelectron momentum spectroscopy of gaseous atoms, e.g., the orbital-dependent observation of lithium (Li) excited states [1], the two-color, core-excitation of neon (Ne) atoms [2], and the xenon Rydberg states [3], to name a few. Resolutions of the photoelectron momentum distribution (PMD) in these experiments are unprecedentedly high, which has made the detailed comparison with theoretical calculations possible.

There are various methods to calculate the PMD of atoms, such as the R-matrix theory [4, 5], the perturbation approach [6], the strong-field approximation [7, 8], and the time-dependent Schrödinger equation (TDSE) [9, 10]. The PMD of hydrogen atoms has been studied extensively in the past using the TDSE [11–14], but the PMD of many-electron atoms previously studied was limited by the single-active-electron (SAE) approximation [3, 15, 16]. One notable exception is the calculation of PMD based on the time-dependent density functional theory (TDDFT) in Ref. [17] using the OCTOPUS code [18], but their method was not tested with real many-electron atoms but with the one-dimensional soft-Coulombic hydrogen atom. The highest-occupied atomic orbitals (HOAOs) of noble-gas atoms beyond the helium (He) are in $p$-states, where the electron-electron interaction forces three degenerate orbitals to be perpendicular to each other, and they ionize by a linearly-polarized laser field into different angles. Since the orbital-dependent measurements of $p$-state PMD are already available [1, 19], theoretical calculations beyond the SAE approximation are urgently needed. Recently, the multi-electron PMDs of noble-gas atoms driven by an extreme ultraviolet (XUV) laser pulse were calculated, based on the solution of the two-electron TDSE in the limit of the frozen-core (FC) approximation [28]. Their calculation was in an excellent agreement with experimental data.

In this paper, we calculate the PMD of He, Ne and argon (Ar) atoms driven by a linearly-polarized visible (527 nm) or near-infrared (800 nm) laser pulse (20 optical cycles in duration), based on the TDDFT. The TDDFT is a mathematically tractable alternative to the many-electron TDSE and assumes a single-electron Hamiltonian for each electron in an atom. The resulting set of linearly independent Kohn-Sham (KS) equations is numerically

solved using the generalized pseudospectral (GPS) method [20]. The KS effective potential of the atom is calculated by using the local density approximation with a self-interaction correction (LDA-SIC) [21]. This scheme has been successfully used in the past to calculate high harmonic spectra of He, Ne and Ar [22] atoms, the strong-field ionization of Li and beryllium atoms [23], the resonance energies of He Rydberg states [24], the Cooper minimum in the high harmonic spectra of an Ar atom [25, 26], and the transient absorption spectra of a He atom [27]. This paper complements these works with the PMD calculation of He, Ne and Ar atoms.

With rapid technological advances in high performance computing, all-electron calculations of atoms in a strong laser field have become as affordable as ever. For the modest-intensity ($0.5 \sim 1 \times 10^{14}$ W/cm$^2$), linearly-polarized driving laser we use in this paper, our TDDFT calculation of the PMD based on the GPS method requires a very moderate number of special points (150-250 radial and 31-63 polar angles) and takes only 5-20 hours per electron per CPU (central processing unit). While we consider the multi-photon ionization of noble-gas atoms driven by a visible-to-infrared (a few eV) laser pulse in our work, the process considered in Ref. [28] is the one-photon double ionization driven by an XUV ($\sim$ 100 eV) laser pulse. In general, the calculation of a one-photon, double ionization requires the $\sim$PW/cm$^2$ driving-laser intensity, which makes our all-electron TDDFT calculation too difficult to converge in a reasonable computation time. Therefore, we restrict our goal in the present paper to the observation of a multi-electron interference effect in a moderately intense, low-frequency driving laser field.

The paper is organized as follows. In Section II, we describe the numerical methods in our calculations. Sec. II A introduces the KS Hamiltonian for the TDDFT based on the LDA-SIC approximation, and Sec. II B and Sec. II C describe the numerical schemes for the initial value problem and the time evolution, respectively. Results are presented in Section III. The PMDs generated by a 527-nm driving laser pulse are discussed first, separately for He (Sec. III A), Ne (Sec. III B) and Ar (Sec. III C) atoms. The PMDs of the Ne and Ar atoms are studied further using an 800-nm laser pulse in Sec. III D. Then, we discuss the applicability of our method to the experiments of Refs. [1] and [19] in Sec. III E. Section IV summarizes the results. Atomic units ($e = m_e = \hbar = 1$) are used throughout, unless specified otherwise.

## II. METHODS

### A. Time-dependent Density Functional Theory

Consider an atom interacting with a strong laser field $\mathbf{E}(t)$. To describe the dynamics of each electron in the atom, we solve the time-dependent KS equation in the length gauge, given by [29]

$$i\frac{\partial}{\partial t}\psi_{i\sigma}(\mathbf{r},t) = \mathcal{H}(\mathbf{r},t)\psi_{i\sigma}(\mathbf{r},t), \tag{1}$$

where $i = 1, 2, ..., N_\sigma$ ranges over occupied atomic orbitals, $\sigma \in \{\uparrow, \downarrow\}$ specifies the electron spin $\pm\frac{1}{2}$, and

$$\mathcal{H}(\mathbf{r},t) = \left[\frac{-1}{2}\nabla^2 - \frac{Z}{r} + v_\sigma^{\mathrm{KS}}[n_\uparrow, n_\downarrow](\mathbf{r},t) + \mathbf{r}\cdot\mathbf{E}(t)\right]. \tag{2}$$

The charge number of a nucleus is equal to the total number of electrons, i.e., $Z = N_\uparrow + N_\downarrow$.

The KS potential $v_\sigma^{\mathrm{KS}}[n_\uparrow, n_\downarrow](\mathbf{r},t)$ in the Hamiltonian $\mathcal{H}(\mathbf{r},t)$ is a functional of the spin electron density

$$n_\sigma(\mathbf{r},t) = \sum_{i=1}^{N_\sigma} n_{i\sigma}(\mathbf{r},t) = \sum_{i=1}^{N_\sigma} |\psi_{i\sigma}(\mathbf{r},t)|^2, \tag{3}$$

and consists of two parts, such that

$$v_\sigma^{\mathrm{KS}}[n_\uparrow, n_\downarrow](\mathbf{r},t) = V_{\mathrm{H}}[n](\mathbf{r},t) + v_\sigma^{\mathrm{xc}}[n_\uparrow, n_\downarrow](\mathbf{r},t). \tag{4}$$

The first term in the above equation is the Hartree potential, defined by

$$V_{\mathrm{H}}[n](\mathbf{r},t) = \iiint \frac{n(\mathbf{r}',t)}{|\mathbf{r}-\mathbf{r}'|} d^3\mathbf{r}', \tag{5}$$

which is a functional of total electron density: $n(\mathbf{r},t) = \sum_\sigma n_\sigma(\mathbf{r},t)$. The second term $v_\sigma^{\mathrm{xc}}[n_\uparrow, n_\downarrow](\mathbf{r},t)$ is an exchange-correlation potential and needs to be approximated in practice. We employ the local density approximation (LDA) with a self interaction correction (SIC) [21, 30]

$$v_\sigma^{\mathrm{xc}}[n_\uparrow, n_\downarrow](\mathbf{r},t) \simeq V_\sigma^{\mathrm{LDA}}[n_\sigma](\mathbf{r},t) - V_\sigma^{\mathrm{SIC}}(\mathbf{r},t), \tag{6}$$

where

$$V_\sigma^{\mathrm{LDA}}[n_\sigma](\mathbf{r},t) = -\left(\frac{6}{\pi} n_\sigma(\mathbf{r},t)\right)^{1/3}, \tag{7}$$

and

$$V_\sigma^{\mathrm{SIC}}(\mathbf{r},t) = V_\sigma^{\mathrm{SI}}(\mathbf{r},t) + \frac{1}{n_\sigma(\mathbf{r},t)} \sum_{i=1}^{N_\sigma}{}' n_{i\sigma}(\mathbf{r},t) v_{i\sigma}(t). \tag{8}$$

In the last expression, $V_\sigma^{\rm SI}(\mathbf{r},t)$ is the self-interaction potential given by

$$V_\sigma^{\rm SI}(\mathbf{r},t) = \frac{1}{n_\sigma(\mathbf{r},t)} \sum_{i=1}^{N_\sigma} n_{i\sigma}(\mathbf{r},t) w_{i\sigma}(\mathbf{r},t), \tag{9}$$

with

$$w_{i\sigma}(\mathbf{r},t) = V_{\rm H}[n_{i\sigma}](\mathbf{r},t) - V_\sigma^{\rm LDA}[n_{i\sigma}](\mathbf{r},t). \tag{10}$$

Moreover, $v_{i\sigma}(t) \equiv \langle V_{i\sigma}^{\rm SIC}(t)\rangle - \langle w_{i\sigma}(t)\rangle$, where

$$\langle V_{i\sigma}^{\rm SIC}(t)\rangle = \iiint V_\sigma^{\rm SIC}(\mathbf{r},t) n_{i\sigma}(\mathbf{r},t)\, d^3\mathbf{r}, \tag{11}$$

and

$$\langle w_{i\sigma}(t)\rangle = \iiint w_{i\sigma}(\mathbf{r},t) n_{i\sigma}(\mathbf{r},t)\, d^3\mathbf{r}. \tag{12}$$

The asymptotic condition, where $V_\sigma^{\rm SIC} \to 0$ as $r \to \infty$, requires that $v_{i\sigma} = 0$ for the HOAOs, and thus the primed summation $\sum'$ in Eq. (8) denotes a summation over all orbitals except for the HOAOs [31]. We can calculate $v_{i\sigma}(t)$ non-iteratively as [32]

$$v_{i\sigma}(t) = \sum_{j=1}^{N_\sigma}{}' [\mathbf{A}_\sigma^{-1}(t)]_{ij} [\langle V_{j\sigma}^{\rm SI}(t)\rangle - \langle w_{j\sigma}(t)\rangle], \tag{13}$$

where

$$[\mathbf{A}_\sigma(t)]_{ij} = \delta_{ij} - \iiint \frac{n_{i\sigma}(\mathbf{r},t) n_{j\sigma}(\mathbf{r},t)}{n_\sigma(\mathbf{r},t)} d^3\mathbf{r}, \tag{14}$$

and

$$\langle V_{j\sigma}^{\rm SI}(t)\rangle = \iiint V_\sigma^{\rm SI}(\mathbf{r},t) n_{j\sigma}(\mathbf{r},t) d^3\mathbf{r}. \tag{15}$$

The LDA-SIC is an exchange-only approximation, so that electrons with opposite spins do not interact. For noble-gas atoms in particular, the number of linearly independent KS equations to be solved is therefore $Z/2$. The total density can then be found by multiplying the spin-up (or -down) electron density by 2.

### B. Initial Value Problem

For the stationary states of atoms, we may assume the separable solution of form

$$\psi_{i\sigma}(\mathbf{r}) = \frac{R_{i\sigma}^\ell(r)}{r} Y_\ell^m(\theta,\phi), \tag{16}$$

where $Y_\ell^m(\theta,\varphi)$ are the spherical harmonics

$$Y_\ell^m(\theta,\varphi) = \sqrt{\frac{(2\ell+1)}{4\pi}\frac{(\ell-m)!}{(\ell+m)!}}\, P_\ell^m(\cos\theta)\, e^{im\phi}, \tag{17}$$

and $P_\ell^m(\cos\theta)$ are the associated Legendre polynomials. Each spin orbital $\psi_{i\sigma}(\mathbf{r})$ is $(2\ell+1)$-fold degenerate for different $m$'s. If we take an average over these degenerate states, then spin electron density of an individual atomic orbital is spherically symmetric and given, by using the addition theorem of spherical harmonics, as

$$\begin{aligned}\bar{n}_{i\sigma}(r) &= \left(\frac{1}{2\ell+1}\right)\frac{|R_{i\sigma}^{\ell}(r)|^2}{r^2}\sum_{m=-\ell}^{\ell}|Y_{\ell m}(\theta,\phi)|^2 \\ &= \frac{|R_{i\sigma}^{(\ell_i)}(r)|^2}{4\pi r^2},\end{aligned} \tag{18}$$

where $\ell_i$ is the angular momentum of $\psi_{i\sigma}(\mathbf{r})$. Note that $\ell_i$ is not a summation index but specific to each $i$-th orbital, and hence we enclose it in parentheses. In the limit of the central field approximation (18), the Hartree potential (5) reduces to a function of only the radial coordinate, i.e.,

$$V_{\rm H}[\bar{n}](r,0) = \int \frac{\bar{n}(r')}{r_>} 4\pi r'^2 dr', \tag{19}$$

where $\bar{n}(r) = \sum_\sigma \sum_{i=1}^{N_\sigma} \bar{n}_{i\sigma}(r)$, and $r_> \equiv \max(r,r')$. The scaled function $U(r) \equiv r V_{\rm H}[\bar{n}](r,0)$ satisfies the following Poisson's equation

$$-\frac{d^2}{dr^2}U(r) = 4\pi r\, \bar{n}(r), \tag{20}$$

with the boundary conditions

$$U(0) = 0, \quad U(r_{\rm max}) = \int_0^{r_{\rm max}} \bar{n}(r)\, 4\pi r^2 dr. \tag{21}$$

In the same limit, the LDA-SIC potential (6) also reduces to a radial function, such that

$$V_\sigma^{\rm LDA}[\bar{n}_\sigma](r,0) = -\left(\frac{6}{\pi}\bar{n}_\sigma(r)\right)^{1/3}, \tag{22}$$

and

$$V_\sigma^{\rm SIC}(r,0) = V_\sigma^{\rm SI}(r,0) + \frac{1}{\bar{n}_\sigma(r)}\sum_{i=1}^{N_\sigma}{}'\bar{n}_{i\sigma}(r) v_{i\sigma}, \tag{23}$$

where

$$V_\sigma^{\rm SI}(r,0) = \frac{1}{\bar{n}_\sigma(r)}\sum_{i=1}^{N_\sigma}\bar{n}_{i\sigma}(r) w_{i\sigma}(r,0), \tag{24}$$

| | | LDA-SIC | KLI | HF | exp. |
|---|---|---|---|---|---|
| He | $1s^2$ | -0.918 | -0.918 | -0.918 | -0.904 |
| | $1s^2$ | -30.836 | -30.802 | -32.772 | 31.976 |
| Ne | $2s^2$ | -1.644 | -1.707 | -1.930 | -1.781 |
| | $2p^6$ | -0.808 | -0.850 | - 0.850 | -0.794 |
| | $1s^2$ | -114.364 | -114.929 | -118.610 | -117.829 |
| | $2s^2$ | -10.981 | -11.958 | -12.322 | -11.991 |
| Ar | $2p^6$ | -8.619 | -9.558 | -9.571 | -9.132 |
| | $3s^2$ | -1.050 | -1.149 | -1.277 | -1.077 |
| | $3p^6$ | -0.549 | -0.630 | -0.591 | -0.581 |

TABLE I. The ground-state energy $\varepsilon_i$ of each bound electron in au, calculated by using the LDA-SIC or the KLI approximations. Also shown are the Hartree Fock results (HF) and experimental values (exp.) from Refs [33] and [34], respectively.

$$w_{i\sigma}(r,0) = V_{\rm H}[\bar{n}_{i\sigma}](r,0) - V_\sigma^{\rm LDA}[\bar{n}_{i\sigma}](r,0), \tag{25}$$

$$v_{i\sigma} = \sum_{j=1}^{N_\sigma}{}'(\mathbf{A}_\sigma^{-1})_{ij}[\langle V_{j\sigma}^{\rm SI}\rangle - \langle w_{j\sigma}\rangle]\,, \tag{26}$$

and

$$(\mathbf{A}_\sigma)_{ij} = \delta_{ij} - \int \frac{\bar{n}_{i\sigma}(r)\bar{n}_{j\sigma}(r)}{\bar{n}_\sigma(r)} 4\pi r^2 dr. \tag{27}$$

Accordingly, the eigenvalue problem for the KS equation (1) becomes diagonal in each $\ell$, such that

$$\mathcal{H}_\ell^0(r) R_{i\sigma}^\ell(r) = \varepsilon_i R_{i\sigma}^\ell(r), \tag{28}$$

where

$$\mathcal{H}_\ell^0(r) = \frac{-1}{2}\frac{\partial^2}{\partial r^2} + \frac{\ell(\ell+1)}{2r^2} - \frac{Z}{r} + v_\sigma^{\rm KS}[\bar{n}_\sigma](r,0), \tag{29}$$

and

$$v_\sigma^{\rm KS}[\bar{n}_\sigma](r,0) = V_{\rm H}[\bar{n}](r,0) + V_\sigma^{\rm LDA}[\bar{n}_\sigma](r,0) - V_\sigma^{\rm SIC}(r,0). \tag{30}$$

Eq. (28) is solved by using the generalized pseudospectral method [20]. The resulting set of eigenvalues and eigenstates are used to construct a time-evolution operator for the stationary part of the Hamiltonian in Eq. (2).

TABLE I lists the groundstate energies $\varepsilon_i$ of occupied atomic orbitals for He, Ne and Ar atoms obtained by the LDA-SIC approximation. In the self-interaction-free theory, the groundstate energy of the HOAOs should be equal to the negative of the first ionization potential [30]. For reference purposes, we calculated the groundstate energies using the Krieger-Li-Iafrate (KLI) approximation [31] as well, whose method is relegated to the Appendix. Also shown are the calculations based on the Hartree-Fock (HF) method from Ref. [33] and the experimental values (exp.) from Ref. [34]. For a comparison of total energies between these methods, see Ref. [21].

### C. TDDFT in a linearly polarized field

Without loss of generality, we may assume that the laser polarization of a linearly-polarized field is along the $z$-axis. Then,

$$E(t) = E_o(t)\sin(\omega_o t) \tag{31}$$

$$\longrightarrow \mathbf{r}\cdot\mathbf{E}(t) = E_o(t)\sin(\omega_o t)\; r\cos\theta, \tag{32}$$

where $E_o(t)$ is a pulse envelope function, given by

$$E_o(t) = \sqrt{I_o}\cos^2\left(\frac{\omega_o\, t}{2n}\right), \tag{33}$$

with $I_o$ and $n$ being the peak intensity and the number of optical cycles ($T = 2\pi/\omega_o$) per pulse, respectively.

Because of the azimuthal symmetry in (32), the magnetic quantum number $m_i$ of the $i$-th orbital is conserved during the time evolution, so that we can assume the solution of form

$$\psi_{i\sigma}(\mathbf{r},t) = \sum_\ell \frac{R_{i\sigma}^{\ell(m_i)}(r,t)}{r} Y_\ell^{(m_i)}(\theta,\phi). \tag{34}$$

It then follows that the spin electron density of each orbital is independent of the azimuthal angle $\phi$ and can be expanded with the Legendre polynomials, such that [35]

$$n_{i\sigma}(r,\theta,t) = \sum_\ell n_{i\sigma}^\ell(r,t)\sqrt{\frac{2\ell+1}{4\pi}}\; P_\ell(\cos\theta), \tag{35}$$

where

$$n_{i\sigma}^\ell(r,t) = \sqrt{\frac{2\ell+1}{4\pi}}\iint d\Omega\; |\psi_{i\sigma}(\mathbf{r},t)|^2\; P_\ell(\cos\theta). \tag{36}$$

Similarly, the Hartree potential of each orbital in a linearly polarized field can also be expanded with the Legendre polynomials as

$$V_{\rm H}[n_{i\sigma}](r,\theta,t) = \sum_{\ell} V_{\ell}^{\rm H}[n_{i\sigma}](r,t)\sqrt{\frac{2\ell+1}{4\pi}}\, P_{\ell}(\cos\theta), \tag{37}$$

where

$$V_{\ell}^{\rm H}[n_{i\sigma}](r,t) = \sqrt{\frac{2\ell+1}{4\pi}} \iint d\Omega\; V_{\rm H}[n_{i\sigma}](r,\theta,t)\; P_{\ell}(\cos\theta). \tag{38}$$

The scaled functions $U_{\ell}(r,t) \equiv r V_{\ell}^{\rm H}[n_{i\sigma}](r,t)$ satisfy the following Poisson's equation

$$\left[-\frac{d^2}{dr^2} + \frac{\ell(\ell+1)}{r^2}\right] U_{\ell}(r,t) = 4\pi r\; n_{i\sigma}^{\ell}(r,t), \tag{39}$$

with the boundary conditions

$$\begin{aligned} U_{\ell}(0,t) &= 0, \\ U_{\ell}(r_{\rm max},t) &= \frac{4\pi}{2\ell+1}(r_{\rm max})^{-\ell}\int_0^{r_{\rm max}} n_{i\sigma}^{\ell}(r,t)\; r^{\ell+2} dr. \end{aligned} \tag{40}$$

The Hartree potential (5) is then found as

$$V_{\rm H}[n](r,\theta,t) = \sum_{\sigma}\sum_{i}^{N_{\sigma}} V_{\rm H}[n_{i\sigma}](r,\theta,t). \tag{41}$$

For the time evolution, the Hamiltonian given by Eq. (2) is split into $\mathcal{H}_{\ell}^{0}(r) + V(r,\theta,t)$, where the stationary Hamiltonian is given by Eq. (29), and

$$\begin{aligned} V(r,\theta,t) = V_{\rm H}[n](r,\theta,t) + V_{\sigma}^{\rm LDA}[n_{\sigma}](r,\theta,t) - V_{\sigma}^{\rm SIC}(r,\theta,t) \\ - v_{\sigma}^{\rm KS}[\bar{n}_{\sigma}](r,0) + E_o(t)\sin(\omega_o t)\; r\cos\theta. \end{aligned} \tag{42}$$

Then, the wavefunction (34) is evolved as [29]

$$\begin{aligned} \psi_{i\sigma}(\mathbf{r}, t+\Delta t) \simeq e^{-i\mathcal{H}_{\ell}^{0}(r)\Delta t/2}\mathcal{L}^{-1}(\ell) e^{-iV(r,\theta,t+\Delta/2)\Delta t} \\ \times \mathcal{L}(\theta) e^{-i\mathcal{H}_{\ell}^{0}(r)\Delta t/2}\psi_{i\sigma}(\mathbf{r},t)\,, \end{aligned} \tag{43}$$

where $\mathcal{L}$ denotes the Legendre transform defined by

$$\begin{aligned} \mathcal{L}\left\{R_{i\sigma}^{\ell(m_i)}(r,t)\right\}(\theta) &\equiv \sum_{\ell} P_{\ell}^{(m_i)}(\theta,\phi)\, R_{i\sigma}^{\ell(m_i)}(r,t) \\ &= \sum_{\ell}\sqrt{\frac{(2\ell+1)(\ell-m_i)!}{2(\ell+m_i)!}} P_{\ell}^{(m_i)}(\cos\theta)\, R_{i\sigma}^{\ell(m_i)}(r,t) \\ &= R_{i\sigma}^{(m_i)}(r,\theta,t). \end{aligned} \tag{44}$$

In the FC approximation, one would neglect the change in the potential that depends on the electron density during the time evolution, so that Eq. (42) reduces to

$$V(r,\theta,t) \simeq E_o(t)\sin(\omega_o t)\, r\cos\theta. \tag{45}$$

In Section III, we will discuss the difference in the PMDs calculated with or without the FC approximation.

In each timestep, the wavefunction $\psi_{i\sigma}(\mathbf{r},t)$ is split into inner and outer regions by a smooth masking function, and the PMD is found from the outer-region wavefunction that is propagated in the momentum space with the Volkov Hamiltonian in the velocity gauge [10, 14]. We study the PMD of each individual electron at the end of the time evolution $t = t_f$, given by

$$D_{i\sigma}(p,\theta_p) = \left|\tilde{\psi}^{\rm v}_{i\sigma}(\mathbf{p},t_f)\right|^2, \tag{46}$$

where $\tilde{\psi}^{\rm v}_{i\sigma}(\mathbf{p},t_f)$ is the Fourier transform of the outer-region wavefunction, as well as the PMD of all electrons, given by

$$D(p,\theta_p) = \left|\sum_{\sigma}\sum_{i=1}^{N_\sigma}\tilde{\psi}^{\rm v}_{i\sigma}(\mathbf{p},t_f)\right|^2. \tag{47}$$

## III. RESULTS

### A. Helium

The total number of electrons in a He atom is $Z = 2$, and therefore only one time-dependent KS equation (1) for one of the two electrons needs to be solved, as the other electron evolves exactly the same way. The TDDFT calculation of a He atom is relatively stable, and the timestep of $\Delta t = 0.2$ is sufficient to obtain converging results.

Figure 1 shows the PMDs of a He atom ($1s^2$) driven by a 527-nm, linearly polarized laser pulse ($n = 20$ optical cycles) of a peak intensity $I_o = 5\times10^{13}$ or $1\times10^{14}$ W/cm$^2$. In Fig. 1, a well-known interference pattern caused by the electron rescattering [11, 16] intercepts the concentric circles of discrete momenta, given by [4]

$$p_s = \sqrt{2(s\,\omega_o + n_o\,\omega_o - I_p - U_p)}, \tag{48}$$

where $s = 1, 2, \ldots$ is the number of above-threshold photons absorbed, $I_p$ is the ionization potential, $U_p = I_o/4{\omega_o}^2$ is the ponderomotive energy, and $n_o = \lfloor I_p/\omega_o \rfloor + 1$. The number

of angular nodes in each concentric circle increases with the driving-laser intensity. The calculation with the FC approximation given by Eq. (45) yields the similar PMDs as Fig. 1, except that the overall PMD yield with the FC approximation is greater than the TDDFT calculation by roughly 10%. This is consistent with the previous TDDFT calculations in Refs. [25, 29], where it was found that the ionization probability of noble-gas atoms according to the TDDFT is smaller than the one based on the FC approximation. To elucidate this point, we integrate the polar angle out of the PMDs with and without the FC approximation and plotted the resulting above-threshold-ionization (ATI) spectra in Figure 2. The first positive photoelectron kinetic energies given by Eq. (48) with an assumption of $I_p = -\epsilon_i$ (the first ionization potential, given in Table I) are 1.96 eV for $I_o = 5 \times 10^{13}$ W/cm$^2$ and 0.66 eV for $I_o = 1 \times 10^{14}$ W/cm$^2$ (and all subsequent spectra are separated by $\omega_o = 2.35$ eV), which agree with the locations of the ATI spectral peaks in Fig. 2.

### B. Neon

For a Ne atom, $Z/2 = 5$ wavefunctions are evolved in total, one electron per spin. The timestep as small as $\Delta t = 0.05$ is necessary to make the TDDFT calculation stable for the $p$-state systems such as Ne or Ar atoms. Figure 3 shows the individual Ne PMDs of $2s$, $2p_0$ and $2p_1$ states in the L-shell, as well as the PMD of all $Z = 10$ states, driven by a 527-nm, linearly polarized, 20-cycle laser pulse of a peak intensity of $I_o = 5 \times 10^{13}$ W/cm$^2$. Because of the symmetry in the Hamiltonian, the $2p_{-1}$ state evolves in the same way as the $2p_1$. The PMD of the $1s$ state is not shown because its photoelectron density turned out negligibly small ($< 10^{-18}$) compared to the other states.

The PMD yield of the Ne($2s$) state in Fig. 3(a) is the smallest, as expected from its relatively large binding energy $-\varepsilon_i$ (see Table I). More strikingly, we find that there is a clear suppression along the $z$-axis in the Ne($2p_1$) PMD in Fig. 3(c), in contrast to the Ne($2p_0$) PMD in Fig. 3(b). This is because the atomic orbital of the $2p_1$ state is aligned in perpendicular to the driving-laser polarization with a node at $z = 0$. One can compare their PMD yield in the ATI spectra in Figure 4. As expected, the spectral intensity of the $2p_0$ state, whose atomic orbital is in parallel with the driving-laser field, is the largest. The first positive photoelectron kinetic energy for the $2p$ state predicted by Eq. (48) is 0.25 eV, which agrees with the ATI peaks of the $2p_0$ and $2p_1$ states in Fig. 4.

It is known that the PMD of the hydrogen atom driven by a linearly polarized laser field has a four-fold symmetry, i.e., $D(r,\theta) = D(r,\pi-\theta) = D(r,-\theta)$ [4]. The He PMDs in Fig. 1 also exhibit such a four-fold symmetry, and so does the PMD of each individual electron of a Ne atom in Figs. 3(a)-(c). On the other hand, the four-fold symmetry is broken in the PMD evaluated from the sum of all states in Fig. 3(d), presumably because of the quantum interference among the complex wavefunctions $\tilde{\psi}^{\rm v}_{i\sigma}(\mathbf{p}, t_f)$ of different phases. A similar effect is known in the high harmonic spectra of the $CO_2$ molecule [36].

### C. Argon

For an Ar atom, $Z/2 = 9$ wavefunctions are evolved. Figure 5 shows the individual Ar PMDs of $3s$, $3p_0$ and $3p_1$ states in the M-shell, as well as the PMD of all $Z = 18$ states. All driving-laser parameters are the same as the Ne calculation in the previous section. The PMDs of the inner atomic orbitals in the K- and the L-shells are not shown, as the electron density in their PMDs turned out negligibly small ($< 10^{-17}$) compared to the M-shell electrons.

Similar to the Ne($2p_1$) PMD in Fig. 3(c), the Ar($3p_1$) PMD in Fig. 5(c) is suppressed along the $z$-axis, whereas the PMDs of $3s$ and $3p_0$ states in Figs. 5(a) and 5(b) are not, reflecting their orbital structures. On the other hand, the intensity of the Ar($3s$) PMD in Fig. 5(a) is fairly large, in contrast to the Ne($2s$) PMD in Fig. 3(a). The PMD yields of different atomic orbitals can be compared with one another in Figure 6, where we plot their corresponding ATI spectra. The intensities of the ATI spectra from degenerate $3p_0$ and $3p_1$ atomic orbitals are particularly close to one another. The first positive photoelectron kinetic energies given by Eq. (48) are 0.72 eV for the $3s^2$ states and 0.23 eV for the $3p^6$ states, in a good agreement with the location of the first spectral peaks in Fig. 6.

The four-fold symmetry we found in the PMDs of each individual atomic orbital in He and Ne atoms also holds for the Ar PMDs in Fig. 5(a)-(c), but it breaks in the PMD of all electrons in Fig. 5(d), similar to the Ne case in Fig. 3(d). Lastly, the Ar($3p_1$) PMD in Fig. 5(c) shows a suppression of electron density in both parallel and perpendicular directions to the laser polarization, resulting in a four-lobe structure; this is consistent with the recent $p$-state measurement of the PMD of krypton atoms during a two-photon ionization (13-eV excitation, followed by a 595-nm linearly-polarized laser pulse) [37].

In Figures 7 and 8, we plot the PMDs and the ATI spectra of an Ar atom calculated with the FC approximation given by Eq. (45). All the laser parameters are kept the same as the TDDFT calculation in Figs. 5 and 6. We find that the PMD yield from the $3s$ state in Fig. 7(a) is negligibly small compared to the one from the $3p_0$ or the $3p_1$ state, in contrast to the TDDFT results in Fig. 5. A comparison of ATI spectra in Fig. 6 and Fig. 8 shows that the FC approximation does not affect the location of ATI spectral peaks but makes the PMD yield from the $3p_0$ state dominate over the other M-shell orbitals ($3s$ and $3p_1$). In view of the electron-electron interaction, inner electrons would ionize more easily after valence electrons ionize, and thus the enhanced ATI yield from the $3s$ state in the TDDFT calculation relative to the FC approximation makes sense.

Another striking difference between the TDDFT and the FC approximation is in the PMD from the Ar($3p_1$) state. Notice that there are 8 angular nodes in the central region of both Fig. 5(c) and Fig. 7(c). While the intensity of each peak separated by these nodes is uniform under the FC approximation in Fig. 7(c), it is weaker in the $z$-direction according to the TDDFT in Fig. 5(c). This is reasonable, given that the electrons in the $3s$ and the $3p_0$ states ionize along the $z$-axis (in parallel with the laser polarization) most in Figs. 5(a) and 5(b). They should interfere with the electrons in the $2p_1$ state from ionizing in the same direction, but the FC approximation fails to predict such electron-electron interaction.

### D. Ionization by infrared lasers

In the previous sections (III A-III C), atoms are driven by a visible (527 nm) linearly-polarized laser pulse. Experimentally, a driving-laser with longer wavelengths (typically near- to mid-infrared) is more commonly used in the momentum spectroscopy [3, 15, 19]. In this section, we study the PMDs of Ne and Ar atoms driven by a near-infrared (800 nm), linearly-polarized 20-cycle laser pulse of a peak intensity $I_o = 1 \times 10^{14}$ W/cm$^2$.

Figure 9 shows the ATI spectra of L-shell and M-shell electrons in Ne and Ar atoms, respectively. The ATI yields from inner electrons are negligibly small ($< 10^{-20}$ for the Ne($1s^2$) states and $< 10^{-15}$ for the Ar($1s^2 2s^2 2p^6$) states) and therefore not shown. We find that the ATI spectral intensities from degenerate $p$-states in Fig. 9 are well separated, and the $m$=0 state that is in parallel with the driving-laser field ($2p_0$ for Ne and $3p_0$ for Ar) yields the most photoelectrons. As a result, it is safe to assume that the SAE approximation is

valid in the PMD calculation with an infrared driving laser field, in accordance with the recent publications by other groups [3, 38]. In Figure 10, we plot the single-electron PMD of the $2p_0$ state of Ne and the $3p_0$ state of Ar. They exhibit complex structures due to the electron rescattering, similar to the xenon PMD measured using a mid-infrared (24-31 $\mu$m) driving laser pulse in Ref. [3].

### E. Discussion

In this section, we would like to discuss the applicability of our current GPS method based on the TDDFT to the experiments in Refs. [1] and [19]. They are two of the earliest measurements of the $p$-state PMDs, resolving the information of different orbitals ($m = 0$ and $\pm 1$). The all-electron calculation of the excited-state Li($1s^2 2p$) PMD, which was measured using an XUV laser pulse (85-91 eV) in Ref. [1], is significantly more complicated than the noble-gas atoms we study in the this paper because (1) the valence shell of a Li atom is partially-filled even in the ground state, which makes the electrons with opposite spins evolve differently, and (2) the stationary-Hamiltonian for the excited-state of a many-electron atom is different from the ground-state calculation in the TDDFT, due to the Kohn-Sham potential which depends on the electron density. Our TDDFT calculation can handle both problems, and our calculation of Li excited states is currently under progress.

There are two reasons why we did not attempt to reproduce the experimental results of Ref. [19]. First, their PMD measurement used a circularly-polarized field, whereas our present TDDFT calculation can only deal with a linearly-polarized laser field, due to the following computational constraints. With a circularly-polarized driving-laser field, the spherical-harmonic expansion of the time-dependent electron density involves complex-valued coefficients, which makes the numerical calculation of a Hartree potential in each timestep significantly more time-consuming than with a linearly-polarized field. Such calculations would be a subject of our future publication.

Second, the main result presented in Ref. [19] was an observation of the quantum beating, where a pump field prepares the initial state as a superposition of two fine-structured states ($^2P_{1/2}$ and $^2P_{3/2}$ of the Ne atom), and a probe field measures the Rabi oscillation of frequency $\tau = 2\pi/\Delta E$, where $\Delta E$ is the fine-structure splitting of the two states. This effect is independent of the probe-field polarization (and the rest of laser parameters such

as intensity, frequency and duration) and happens as long as the initial state is prepared as a superposition of two states with different energies. In fact, Ref. [19] demonstrated the Rabi oscillation between the two fine-structure states using a linearly-polarized field as well. Furthermore, this type of quantum beating is not restricted to the fine-structure states but can happen between any two non-degenerate eigenstates, as evidenced in Ref. [39] where the quantum beating between various excited states of a He atom was measured. Ref. [39] also presents a TDSE calculation in the limit of the SAE approximation, which reproduces the quantum beating in their experiment; in this sense, the quantum beating in Ref. [19] is not a multi-electron effect we aimed to study in our present work. This was the second reason why we did not attempt a direct comparison between our calculation and the experimental results in Ref. [19]. A theoretical calculation was given in Ref. [19] based on the rotating wave approximation for a two-level system, which was sufficient to explain the quantum beating. It would be more desirable, however, to diagonalize the stationary-state Hamiltonian in the $(j, m_j)$-basis rather than the $(\ell, m)$-basis in the GPS method, to take the fine structure into account.

## IV. CONCLUSION

In this paper, we calculated the photoelectron momentum distribution (PMD) of noble-gas atoms (He, Ne and Ar) driven by a linearly-polarized 20-cycle laser pulse of peak intensities $0.5 \sim 1 \times 10^{14}$ W/cm$^2$ based on the time-dependent density functional theory (TDDFT). With a visible (527 nm) driving-laser frequency, we find that the PMD yields from outer orbitals according to the TDDFT are comparable in strengths, so that they could interfere and break the four-fold symmetry in the PMDs. This is an example of the quantum interference due to different complex phases among the individual wavefunctions in an atom. There are no experimental data to compare our results with yet, but such a symmetry breaking should exist in the PMD of multi-electron atoms driven at a visible (400-700 nm) laser frequency. To observe the many-electron interference effect, it is crucial that the spectral intensities of multiple orbitals are comparably strong. For a longer ($\sim$ 800 nm) driving-laser frequency, which is more commonly used in the PMD experiments, we found that the PMDs of degenerate $p$-state orbitals are well separated in their intensities, so that the interference effect is not observable. Moreover, the PMDs of $p$-state electrons with $m = \pm 1$ are suppressed along

the $z$-axis, reflecting their orbital orientations and the interference with the $m$=0 electron that mostly ionizes along the $z$-axis. Therefore, when driven by a linearly-polarized field at an infrared driving-laser frequency, the PMD yield from the outermost electron with $m = 0$ dominates over the rest of the electrons, so that one can safely adapt the SAE approximation to calculate the PMD.

## ACKNOWLEDGMENTS

This work was partially supported by the U.S. Department of Energy under Contract No. DE-FG02-06ER46304 (MM and GPZ) and by the Chemical Sciences, Geosciences and Biosciences Division of the Office of Basic Energy Sciences, Office of Science, US Department of Energy (SIC). MM and SIC also acknowledge partial support from the Ministry of Science and Technology of Taiwan and National Taiwan University (Grant No. 06R104021 and No. 106R8700-2). Numerical calculation was done on Indiana State University's quantum cluster and high-performance computer (obsidian). The research used resources of the National Energy Research Scientific Computing Center, which is supported by the Office of Science of the U.S. Department of Energy under Contract No. DE-AC02-05CH11231.

## APPENDIX

The Krieger-Li-Iafrate (KLI) approximation [31] is an exchange-only KS potential for the stationary-state of a many-electron atom, given by

$$v_\sigma^{\rm xc}[n_\uparrow, n_\downarrow](\mathbf{r}) \simeq V_\sigma^{\rm S}(r) + \frac{1}{\bar{n}_\sigma(r)} \sum_{i=1}^{N_\sigma} \bar{n}_{i\sigma}(r) v_{i\sigma}, \tag{A-1}$$

where $V_\sigma^{\rm S}$ is the Slater potential defined by

$$V_\sigma^{\rm S}(r) = \frac{1}{\bar{n}_\sigma(r)} \sum_{i=1}^{N_\sigma} \bar{n}_{i\sigma}(r) v_{i\sigma}^{\rm HF}(r), \tag{A-2}$$

with $v_{i\sigma}^{\rm HF}$ being the single-particle Hartree-Fock exchange potential

$$v_{i\sigma}^{\rm HF}(r) = \frac{-1}{R_{i\sigma}^{(\ell_i)}(r)} \sum_{j=1}^{N_\sigma} R_{j\sigma}^{(\ell_j)}(r) \sum_{\ell=|\ell_i-\ell_j|}^{\ell_i+\ell_j} \begin{pmatrix} \ell_i & \ell_j & \ell \\ 0 & 0 & 0 \end{pmatrix}^2 W_{ij}^{\sigma,\ell}(r). \tag{A-3}$$

In the above expression, $R_{i\sigma}^{(\ell_i)}(r)$ is the radial function in Eq. (16), $\left(\begin{smallmatrix}\ell_i & \ell_j & \ell \\ 0 & 0 & 0\end{smallmatrix}\right)$ are Wigner-3j coefficients, and

$$W_{ij}^{\sigma,\ell}(r) \equiv \int \frac{{r_<}^{\ell}}{{r_>}^{\ell+1}} R_{i\sigma}^{(\ell_i)}(r') R_{j\sigma}^{(\ell_j)}(r') dr', \tag{A-4}$$

with $r_< \equiv \min(r, r')$ and $r_> \equiv \max(r, r')$. In practice, $W_{ij}^{\sigma,\ell}(r)$ is obtained by solving the following differential equation:

$$\left[-\frac{d^2}{dr^2} + \frac{\ell(\ell+1)}{r^2}\right] Q_{ij}^{\sigma,\ell}(r) = (2\ell+1) \frac{R_{i\sigma}^{(\ell_i)}(r) R_{j\sigma}^{(\ell_j)}(r)}{r}, \tag{A-5}$$

where $Q_{ij}^{\sigma,\ell}(r) \equiv r W_{ij}^{\sigma,\ell}(r)$. The boundary conditions are

$$\begin{aligned} Q_{ij}^{\sigma,\ell}(0) &= 0, \\ Q_{ij}^{\sigma,\ell}(r_{\max}) &= \begin{cases} \delta_{ij} & \text{if } \ell = 0 \\ \frac{1}{(r_{\max})^{\ell}} \int_0^{r_{\max}} R_{i\sigma}^{(\ell_i)}(r) R_{j\sigma}^{(\ell_j)}(r)\, r^{\ell} dr & \text{otherwise.} \end{cases} \end{aligned} \tag{A-6}$$

The orbital-dependent constant $v_{i\sigma}$ in Eq. (A-1) is found as

$$C_{i\sigma} \equiv \langle V_{i\sigma}^{\mathrm{KLI}} \rangle - \langle v_{i\sigma}^{\mathrm{HF}} \rangle = \sum_{j=1}^{N_\sigma} (\mathbf{A}_\sigma^{-1})_{ij} [\langle V_{j\sigma}^{\mathrm{S}} \rangle - \langle v_{j\sigma}^{\mathrm{HF}} \rangle], \tag{A-7}$$

where $\mathbf{A}_\sigma$ is given by Eq. (27).

---


[1] G. Zhu, M. Schuricke, J. Steinmann, J. Albrecht, J. Ullrich, I. Ben-Itzhak, T. J. M. Zouros, J. Colgan, M. S. Pindzola, and A. Dorn, Phys. Rev. Lett. **103**, 103008 (2009).

[2] M. Meyer, P. Radcliffe, T. Tschentscher, J. T. Costello, A. L. Cavalieri, I. Grguras, A. R. Maier, R. Kienberger, J. Bozek, C. Bostedt, S. Schorb, R. Coffee, M. Messerschmidt, C. Roedig, E. Sistrunk, L. F. DiMauro, G. Doumy, K. Ueda, S. Wada, S. Dusterer, A. K. Kazansky, and N. M. Kabachnik, Phys. Rev. Lett. **108**, 063007 (2012).

[3] Y. Huismans, A. Rouzee, A. Gijsbertsen, P. S. W. M. Logman, F. Lepine, C. Cauchy, S. Zamith, A. S. Stodolna, J. H. Jungmann, J. M. Bakker, G. Berden, B. Redlich, A. F. G. van der Meer, K. J. Schafer, and M. J. J. Vrakking, Phys. Rev. A **87**, 033413 (2013).

[4] S. Basile, F. Trombetta, and G. Ferrante, Phys. Rev. Lett. **61**, 2435 (1988).

[5] L. R. Moore, M. A. Lysaght, J. S. Parker, H. W. van der Hart, and K. T. Taylor, Phys. Rev. A **84**, 061404(R) (2011).

[6] A. N. Grum-Grzhimailo and E. V. Gryzlova, Phys. Rev. A **89**, 043424 (2014).

[7] A. K. Kazansky, I. P. Sazhina, and N. M. Kabachnik, Phys. Rev. A **82**, 033420 (2010).

[8] M. Klaiber, K. Z. Hatsagortsyan, and C. H. Keitel, Phys. Rev. Lett. **114**, 083001 (2015).

[9] K. J. Schafer, B. Yang, L. F. DiMauro, and K. C. Kulander, Phys. Rev. Lett. **70**, 1599 (1993).

[10] X. M. Tong, K. Hino, and N. Toshima, Phys. Rev. A **74**, 031405(R) (2006).

[11] D. G. Arbo, S. Yoshida, E. Persson, K. I. Dimitriou, and J. Burgdorfer, Phys. Rev. Lett. **96**, 143003 (2006).

[12] D. A. Telnov and S.-I. Chu, Phys. Rev. A **79**, 043421 (2009).

[13] M. F. Ciappina, J. A. Perez-Hernandez, T. Shaaran, L. Roso, and M. Lewenstein, Phys. Rev. A **87**, 063833 (2013).

[14] M. Murakami and S.-I. Chu, Phys. Rev. A **93**, 023425 (2016).

[15] M. Schuricke, G. Zhu, J. Steinmann, K. Simeonidis, I. Ivanov, A. Kheifets, A. N. Grum-Grzhimailo, K. Bartschat, A. Dorn, and J. Ullrich, Phys. Rev. A **83**, 023413 (2011).

[16] Z. Chen, T. Morishita, A.-T. Le, M. Wickenhauser, X. M. Tong, and C. D. Lin, Phys. Rev. A **74**, 053405 (2006).

[17] U. D. Giovannini, D. Varsano, M. A. L. Marques, H. Appel, E. K. U. Gross, and A. Rubio, Phys. Rev. A **85**, 062515 (2012).

[18] M. Marques, A. Castro, G. F. Bertsch, and A. Rubio, Computer Physics Communications **151**, 60 (2003).

[19] A. Fleischer, H. J. Wörner, L. Arissian, L. R. Liu, M. Meckel, A. Rippert, R. Dörner, D. M. Villeneuve, P. B. Corkum, and A. Staudte, Phys. Rev. Lett. **107**, 113003 (2011).

[20] X.-M. Tong and S.-I. Chu, Chemical Physics **217**, 119 (1997).

[21] X.-M. Tong and S.-I. Chu, Phys. Rev. A **55**, 3406 (1997).

[22] X.-M. Tong and S.-I. Chu, Phys. Rev. A **64**, 013417 (2001).

[23] D. A. Telnov, J. Heslar, and S.-I. Chu, Chemical Physics **391**, 88 (2011).

[24] J. Heslar and S.-I. Chu, Phys. Rev. A **86**, 032506 (2012).

[25] D. A. Telnov, K. E. Sosnova, E. Rozenbaum, and S.-I. Chu, Phys. Rev. A **87**, 053406 (2013).

[26] P.-C. Li and S.-I. Chu, Phys. Rev. A **88**, 053415 (2013).

[27] J. Heslar, D. A. Telnov, and S.-I. Chu, Phys. Rev. A **89**, 052517 (2014).

[28] F. L. Yip, T. N. Rescigno, C. W. McCurdy, and F. Martín, Phys. Rev. Lett. **110**, 173001 (2013).

[29] X.-M. Tong and S.-I. Chu, Phys. Rev. A **57**, 452 (1998).

[30] J. P. Perdew and A. Zunger, Phys. Rev. B **23**, 5048 (1981).

[31] J. B. Krieger, Y. Li, and G. J. Iafrate, Phys. Rev. A **46**, 5453 (1992).

[32] C. A. Ullrich, U. J. Gossmann, and E. K. U. Gross, Phys. Rev. Lett. **74**, 872 (1995).

[33] C. F. Bunge and J. A. Barrientos, Atomic Data and Nuclear Data Tables **53**, 113 (1993).

[34] K. D. Sevier, Atomic Data and Nuclear Data Tables **24**, 323 (1979).

[35] T. F. Jiang, X.-M. Tong, and S.-I. Chu, Phys. Rev. B **63**, 045317 (2001).

[36] O. Smirnova, Y. Mairesse, S. Patchkovskii, N. Dudovich, D. Villeneuve, P. Corkum, and M. Y. Ivanov, Nature **460**, 08253 (2009).

[37] N. Saquet, D. M. P. Holland, S. T. Pratt, D. Cubaynes, X. Tang, G. A. Garcia, L. Nahon, and K. L. Reid, Phys. Rev. A **93**, 033419 (2016).

[38] X.-M. Tong, G. Wachter, S. A. Sato, C. Lemell, K. Yabana, and J. Burgdorfer, Phys. Rev. A **92**, 043422 (2015).

[39] N. Shivaram, X.-M. Tong, H. Timmers, and A. Sandhu, J. Phys. B: At. Mol. Opt. Phys. **49**, 055601 (2016).

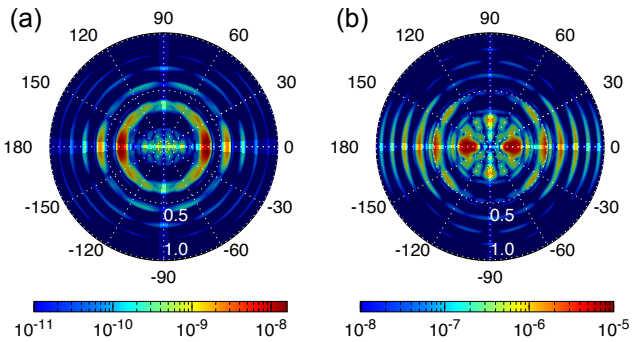


FIG. 1. (Color online) The cross section of photoelectron momentum distributions (PMDs) of a He atom, driven by the 527-nm, linearly polarized, 20-cycle laser pulse along the $z$-axis with the peak intensity of (a) $I_o = 5 \times 10^{13}$ W/cm$^2$ or (b) $1 \times 10^{14}$ W/cm$^2$. The PMD intensity is in the logarithmic scale and shown as a color map.

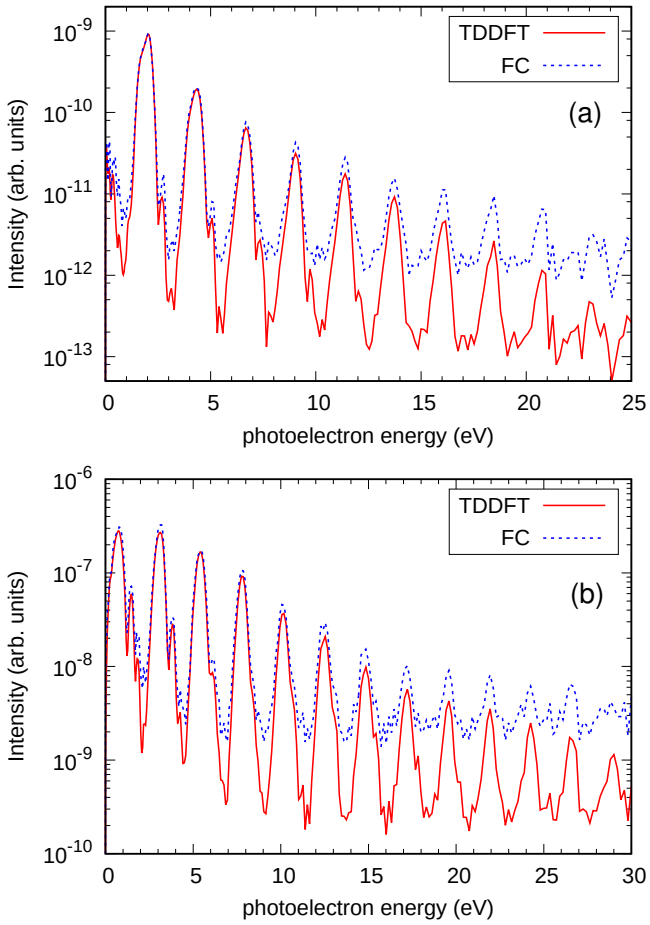


FIG. 2. (Color online) The above-threshold-ionization (ATI) spectra of a He atom, obtained by integrating the polar angle out of the PMDs in Fig. 1, are shown with solid lines (TDDFT) for (a) $I_o = 5 \times 10^{13}$ W/cm$^2$ and (b) $I_o = 1 \times 10^{14}$ W/cm$^2$. Also shown with dotted lines are the spectra from the frozen-core (FC) approximation.

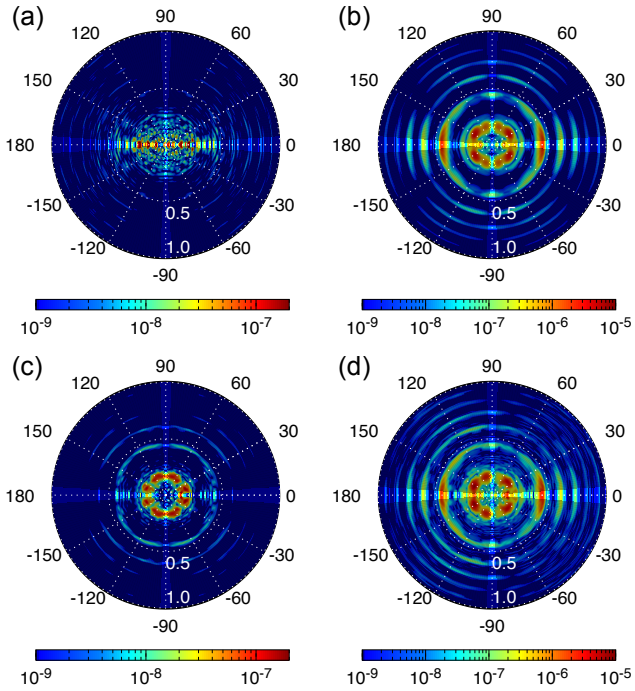


FIG. 3. (Color online) The PMD cross section of a Ne atom, driven by the 527-nm, linearly polarized, 20-cycle laser pulse along the $z$-axis with the peak intensity of $I_o = 5 \times 10^{13}$ W/cm$^2$, obtained from (a) the $2s$ state, (b) the $2p_0$ state, (c) the $2p_1$ state, and (d) the sum of all ($1s^2 2s^2 2p^6$) states.

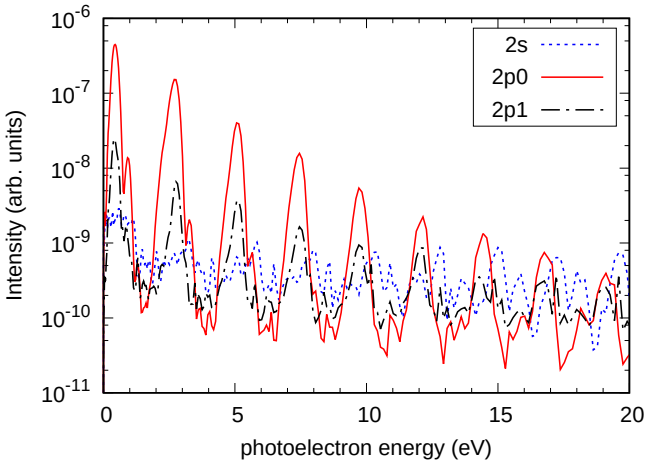


FIG. 4. (Color online) The ATI spectra of a Ne atom, obtained by integrating the polar angle out of the PMDs in Figs. 3(a)-(c).

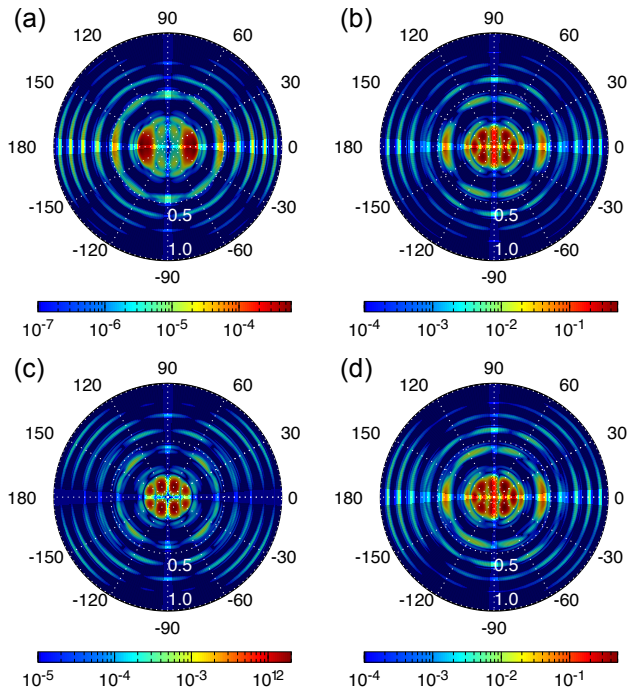


FIG. 5. (Color online) The PMD cross section of an Ar atom, driven by the 527-nm, linearly polarized, 20-cycle laser pulse along the $z$-axis with the peak intensity of $I_o = 5 \times 10^{13}$ W/cm$^2$, obtained from (a) the $3s$ state, (b) the $3p_0$ state, (c) the $3p_1$ state, and (d) the sum of all $(1s^2 2s^2 2p^6 3s^2 3p^6)$ states.

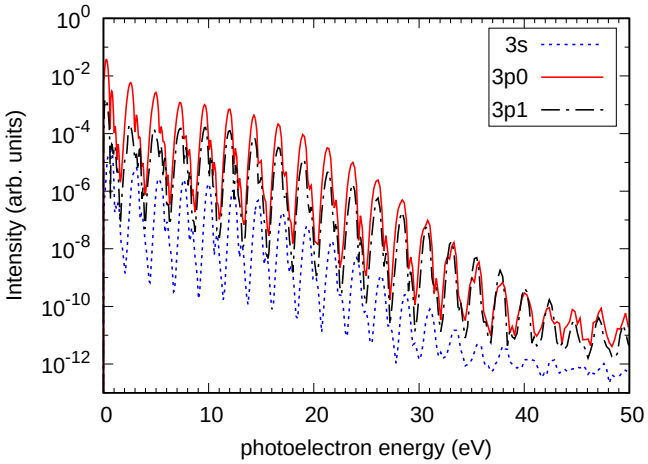


FIG. 6. (Color online) The ATI spectra of an Ar atom, obtained by integrating the polar angle out of the PMDs in Figs. 5(a)-(c).

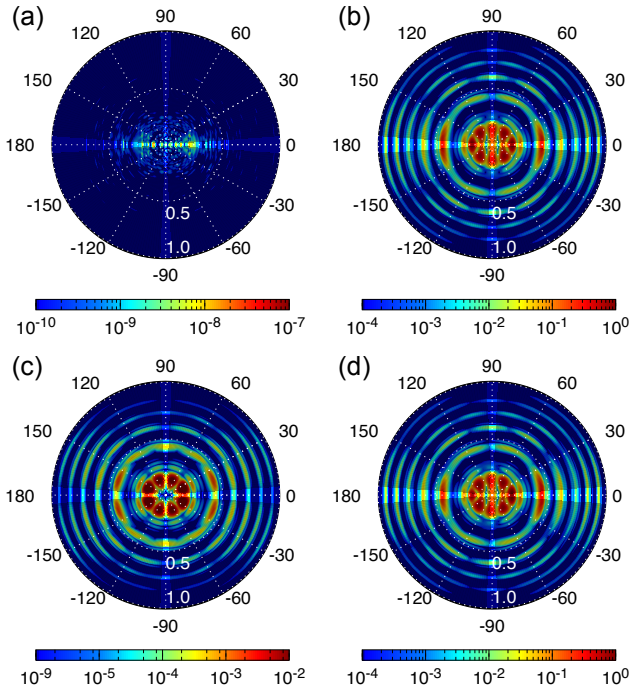


FIG. 7. (Color online) The same as Fig. 5, but calculated with the frozen-core approximation.

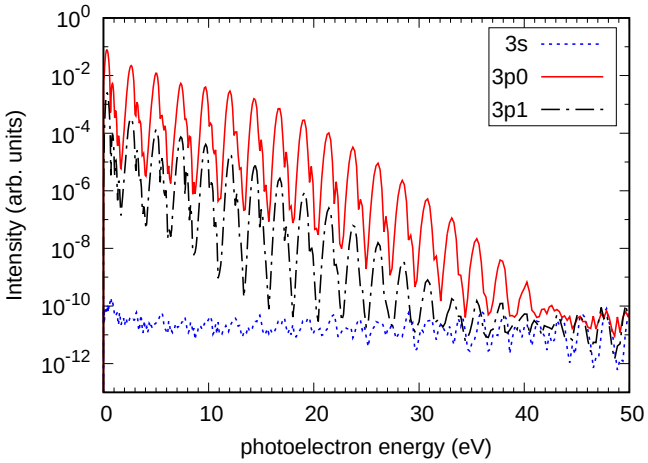


FIG. 8. (Color online) The ATI spectra of an Ar atom under the frozen-core approximation, obtained by integrating the polar angle out of the PMDs in Fig. 7.

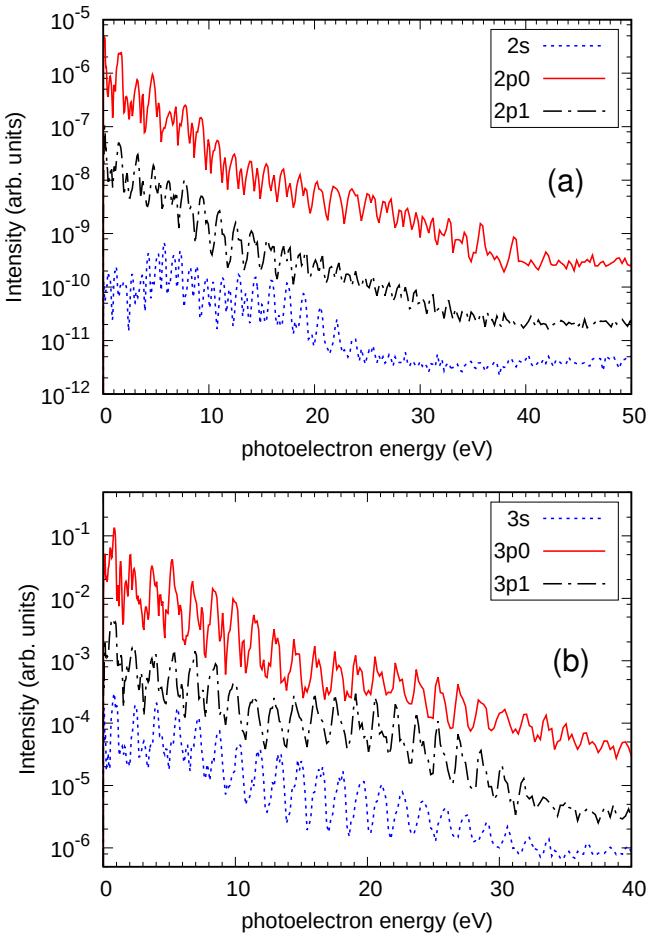


FIG. 9. (Color online) The ATI spectra from (a) the L-shell electrons of a Ne atom and (b) the M-shell electrons of an Ar atom, driven by an 800-nm, linearly polarized, 20-cycle laser pulse along the $z$-axis with the peak intensity of $1 \times 10^{14}$ W/cm$^2$.

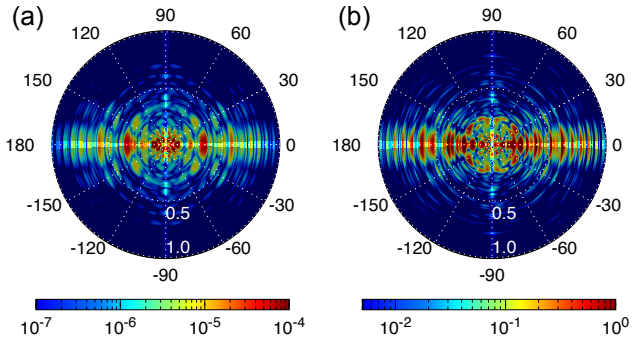


FIG. 10. (Color online) The PMD cross section of (a) the Ne($2p_0$) state and (b) the Ar($3p_0$) state in Fig. 9.